

Toward Conductive Mesocrystalline Assemblies: PbS Nanocrystals Cross-Linked with Tetrathiafulvalene Dicarboxylate

Alexander André,[†] Danylo Zhrebetskyy,[‡] David Hanifi,^{¶,‡} Bo He,[¶] Mahdi Samadi Khoshkhoo,[†] Maciej Jankowski,^{||} Thomas Chassé,^{†,‡} Lin-Wang Wang,[‡] Frank Schreiber,^{‡,§} Alberto Salleo,[#] Yi Liu,[¶] and Marcus Scheele^{*,†,‡}

[†]Institute of Physical and Theoretical Chemistry; [‡]Center for Light–Matter Interaction, Sensors, and Analytics LISA+; and [§]Institute of Applied Physics, University of Tübingen, 72076 Tübingen, Germany

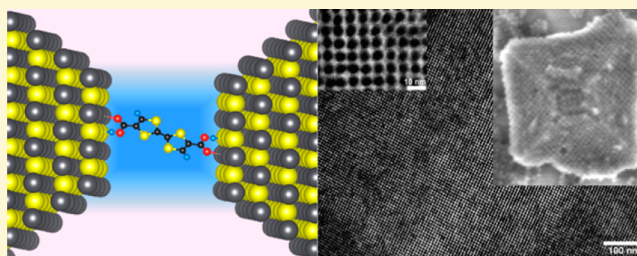
[‡]Material Sciences Division and [¶]Molecular Foundry, Lawrence Berkeley National Laboratory, Berkeley, California 94720, United States

[#]Department of Materials Science and Engineering, Stanford University, 476 Lomita Mall, Stanford, California 94305, United States

^{||}Beamline ID03, European Synchrotron Radiation Facility (ESRF), Grenoble F-38043, France

Supporting Information

ABSTRACT: We use the organic semiconductor tetrathiafulvalene dicarboxylate (TTFDA) to assemble PbS nanocrystals into conductive mesocrystals. Density functional theory calculations predict a size-tunable, near-resonant alignment between the PbS $1S_{\text{h}}$ state and the TTFDA HOMO with the potential to form a conductive channel for holes. We test this hypothesis with transport measurements on TTFDA-functionalized PbS nanocrystals of different sizes and find a pronounced modulation of the field-effect hole mobilities. Photothermal deflection spectroscopy reveals unchanged Urbach energies after ligand exchange, whereas further surface modification by colloidal-atomic layer deposition leads to a strong increase in the density of in-gap states. Hole transport in PbS-TTFDA is unusually robust against such surface modification. Our structural analysis of the mesocrystals suggests that TTFDA induces a defined interparticle spacing, the orientation of atomic lattices, and the angle within the mesocrystal unit cell. The results of this work pave the way toward conductive mesocrystalline assemblies of hybrid semiconductor nanostructures with size-tunable transport properties.



Coupled organic–inorganic nanostructures (COINs) utilize organic semiconductors (OSCs) to facilitate charge carrier transport through nanocrystal (NC) ensembles by exploiting resonances in relevant energy levels between the NC and OSC.¹⁸ By replacing the native NC ligand with an OSC, adjacent NCs are cross-linked, and dense solids of NC–OSC hybrids with rigid interparticle spacings are formed.⁴² These spacings are often significantly wider than those imposed by ligand exchange strategies operating with short insulating molecules like 1,2-ethanedithiol, hydrazine, or halides owing to the rigid and relatively long (≥ 1.0 nm) OSC molecules.^{1,7,38} An inherent problem with NCs modified by such short ligand exchange strategies is the strong increase in fast and nonradiative recombination pathways with decreasing interparticle spacing.⁴⁵ Furthermore, it is challenging to maintain crack-free NC solids with long-range order due to the large volume contraction upon ligand exchange with short molecules, which is crucial for efficient transport.^{2,7} In this respect, COINs offer the perspective to combine efficient charge carrier transport with a high degree of structural order, which is otherwise difficult to realize.

For an NC solid with a significant amount of in-film order, another important question is the degree of orientational order. If the atomic lattices of individual NCs within an ordered array of NCs are randomly oriented, the assembly is nondirectional, while for perfectly iso-oriented NCs, the lattice is said to be “mesocrystalline”.^{3,19} Mesocrystalline assemblies of NCs functionalized with long-chained and insulating organic molecules (e.g., oleic acid) have been reported by several groups, but these NC ensembles are typically insulating.^{4,5,25–28} For conductive mesocrystals, it is expected that carrier transport is highly direction dependent due to different spatial orientations of the electron- and hole-wave function. For instance, cuboctahedral PbSe NCs are predicted to show preferential hole transport along the [001]-direction and good electron coupling along the [111] direction.⁶ It is therefore highly desirable to achieve electronic coupling and mesocrystalline assembly in an NC solid simultaneously. Weidman et al. have shown that under certain circumstances, iso-orientation of

Received: September 28, 2015

Revised: November 12, 2015

Published: November 12, 2015

NCs can also be partially preserved upon ligand exchange with small molecules like 3-mercaptopropionic acid, but further studies are clearly in place to work toward conductive mesocrystalline NC assemblies.⁷

Here, we report on PbS NC solids cross-linked with the OSC tetrathiafulvalene dicarboxylate (TTFDA). We demonstrate that this molecule invokes a mesocrystalline assembly of PbS NCs into a near-cubic close-packed structure in which the atomic lattices are strictly coaligned with the NC lattices. The mesocrystalline structure is already observed in the first NC monolayer indicating that strong in-plane interactions are responsible for the observed packing. The interparticle distance along the [001] direction of the NC lattice coincides with the length of TTFDA implying that the NCs are separated by one monolayer of the OSC. Our results are supported by optical spectroscopy and density functional theory (DFT). The latter is also used to predict the transport properties of this COIN, which are found to be dominated by a weak resonance for holes, especially for larger NC diameters. This is confirmed by field-effect transistor (FET) measurements revealing unipolar hole conduction with a 40-fold increase in mobility as the NC diameter is increased from 6.3 to 9.7 nm.

RESULTS

Five samples of PbS NCs capped with Pb[oleate]₂/Cl⁻ with varying diameters between 5.0 and 9.7 nm and tetrabutylammonium tetrathiafulvalenedicarboxylate ([TBA]₄TTFDA) are synthesized following a previously published procedure.⁸ The mean NC diameters and standard deviations are obtained from transmission electron microscopy (TEM) images on counting at least 200 NCs per sample, assuming a circular shape (or spherical in 3D), and calculating the nominal diameter from the area covered by the particle. In accordance with previous works operating with the same synthetic procedure, the typical NC shape in all samples is a cuboctahedron composed of six {001} and eight {111} facets, such that the assumption of a sphere is a first-order approximation for simplicity.⁹

[TBA]₄TTFDA is soluble in a variety of common polar solvents such as alcohols, acetonitrile, and also chloroform, but not toluene or hexanes. The optical absorption spectrum in methanol (Figure 1a) bears large similarities with the recently

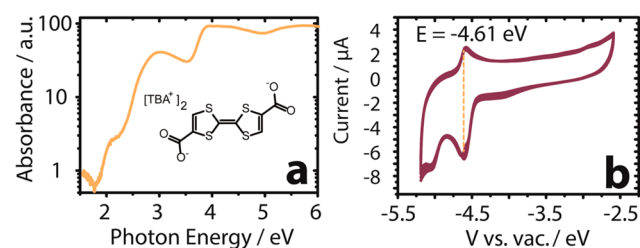


Figure 1. (a) Optical absorption of a solution of [TBA]₄TTFDA in methanol. (b) Cyclovoltammetric scan of [TBA]₄TTFDA in methanol. The redox wave of the HOMO (indicated by the dashed line) is referenced against the ferrocene/ferrocenium redox couple to extract the HOMO position with respect to the energy of free space.

investigated tetracarboxylate analogue (TTFTA).¹⁸ The LUMO ← HOMO transition is probably the band at ~2.9 eV, while the weak absorption at ~2.2 eV is due to the readily formed radical.¹⁰ Cyclic voltammetry (CV) in a methanol solution of tetrabutylammonium hexafluorophosphate reveals a reversible redox wave at -0.29 V against ferrocene/ferrocenium

(Fc/Fc⁺) as an internal standard. Setting Fc/Fc⁺ to -4.90 eV versus the absolute vacuum level allows us to infer a HOMO position at -4.61 eV versus vacuum (Figure 1b).¹¹ This is almost identical to the recently investigated [TBA]₄TTFTA (-4.64 eV vs vac) and within the experimental error, highlighting again the similarities between both molecules.

Ligand exchange with [TBA]₂TTFDA is carried out either at the solid/air interface by using orthogonal solvents (“solid/air exchange”) or by a Langmuir-type “liquid/air exchange” as detailed in the Methods. The effect of the ligand exchange is monitored in Figure 2. X-ray photoemission spectroscopy (XPS) in the S 2p (Figure 2a) and S 2s (Figure 2b) spectral region of the same PbS NC sample (1) before and (2) after exchange with [TBA]₂TTFDA reveals the occurrence of a second sulfur species at higher binding energy (164 and 228 eV) than the sulfur species in PbS (161 and 226 eV). In accordance with previous XPS results on P3HT (doublet at 164.5 and 165.5 eV), which provides a similar chemical environment for the S 2p core levels, we attribute this new sulfur species to TTFDA on the surface of PbS NCs.¹² The S 2p core level of the PbS NCs before ligand exchange is also in good agreement with previous results on bulk PbS (S 2p_{3/2} = 161.0 eV).¹³

The exchange is further monitored with Fourier transform infrared (FT-IR) spectroscopy in Figure 2, panel c. The vibrational spectrum of PbS NCs surface-functionalized with Pb[oleate]₂ (1) displays strong sp³ C–H vibrations ≤3000 cm⁻¹ as well as a barely visible sp² C–H vibration above 3000 cm⁻¹. The C=O vibrations expected around 1700 cm⁻¹ are substantially weakened and shifted to smaller wavenumbers (1570 and 1460 cm⁻¹), which is often attributed to a binding interaction with the particles’ surface. Upon ligand exchange with [TBA]₂TTFDA (2), the spectrum changes, especially in the fingerprint region. Several new bands occur, particularly at 1720 cm⁻¹, 1550 cm⁻¹, 1360 cm⁻¹, and 1250 cm⁻¹, which are not part of the previous spectrum. The sp³ C–H vibrations have effectively vanished, indicating a near-complete ligand exchange. As illustrated in Figure 2, panel d, the expected exchange reaction involves a replacement of the TBA⁺ cation with Pb²⁺, previously bound to oleate, and [TBA]oleate as the leaving species.¹⁴ Therefore, for a fully exchanged PbS NC film without residual, unbound [TBA]₂TTFDA (Figure 2c, 3), there should be no bands in the spectral regime just under 3000 cm⁻¹. The unsaturated C–H vibration is probably too weak to be clearly observed in this film. In conclusion, both XPS and FT-IR data indicate a near-complete replacement of the Pb[oleate]₂ ligand shell with Pb[TTFDA].

The first excited hole state (1S_h) of PbS NCs has been measured by several groups for various sizes and surface functionalization.^{15–17} It is typically found at about -5.0 eV versus vacuum, but the exact position is slightly size-dependent and strongly influenced by the surface ligand. To address this issue, we have carried out DFT calculations of a 10 nm PbS NC in the vicinity of TTFDA. While a detailed description of the procedure may be found in the Supporting Information, here we only outline the most fundamental points. Since the NCs pack in a near-cubic structure (Figure 4), the {001} facets are the most relevant facets of interaction and charge transport between the NCs; interactions through the {111} would have hexagonal packing. Therefore, a PbS NC is mimicked by a slab of the {001} facet interacting with TTFDA (see the structural investigations in Figure 4), to which TTFDA is attached and allowed to relax into the energetically most favorable

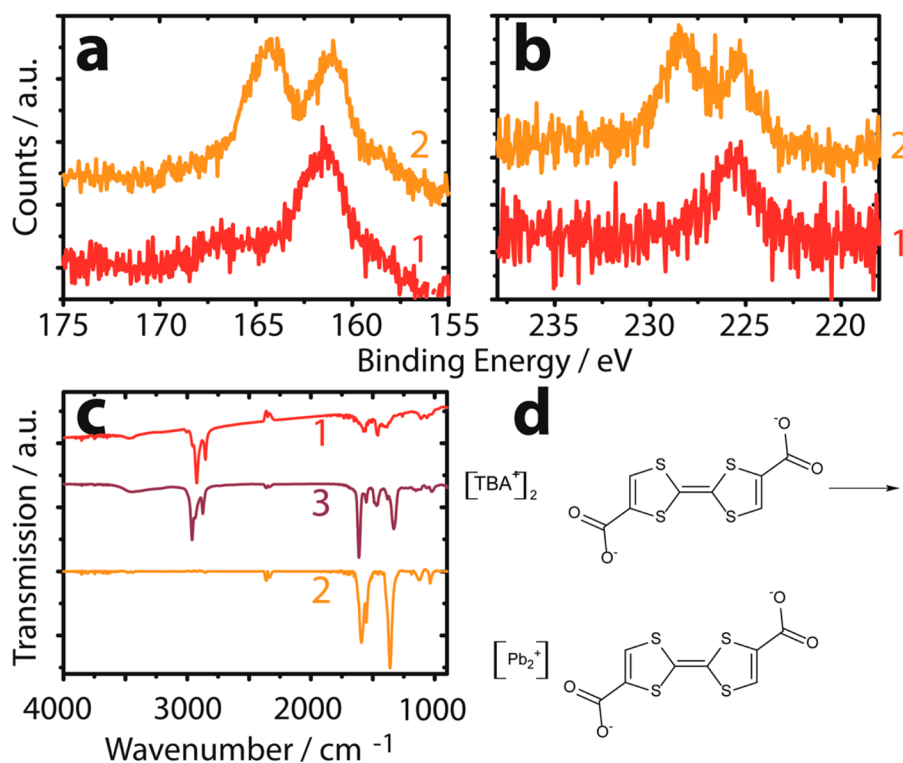


Figure 2. (a) XPS spectra of the S 2p region and (b) of the S 2s region of (1) PbS NCs functionalized with Pb[oleate]₂, (2) PbS NCs after ligand exchange with TTFDA. (c) FT-IR spectra of the same compounds including pure [TBA]₂TTFDA (3). (d) Chemical scheme of the ligand exchange process.

configuration. The absolute energies of the states ($1S_h/1S_e$ for the NC, HOMO/LUMO for TTFDA) are calculated by the Heyd–Scuseria–Ernzerhof functional (HSE03). To account for the electronic interaction between the two semiconductors upon binding, spin–orbit coupling and quantum confinement in the NC, a variety of corrections need to be applied to the results obtained with HSE03, similarly to a previously described procedure.¹⁸ The results (Figure 3a) predict a $1S_h-1S_e$ gap for the NC of ~ 1.2 eV and a HOMO–LUMO gap of ~ 3.2 eV, which compares to ~ 0.6 eV and ~ 2.9 eV by optical spectroscopy, respectively. However, optical spectroscopy of the pure compounds underestimates the energy gap by the

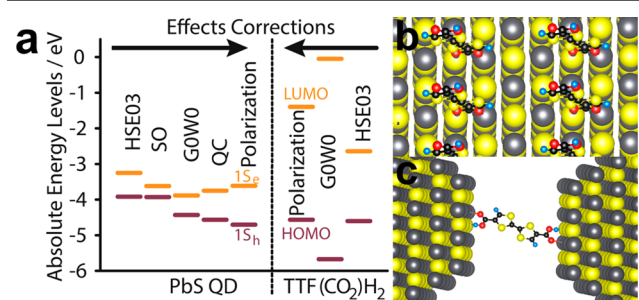


Figure 3. (a) Calculated energy levels of a 10 nm PbS nanoparticle (left) and a TTFDA molecule (right). The final energy levels are the offsets next to the dashed line, which are obtained by starting with a hybrid HSE03 corrected relative to vacuum level and consecutively taking into account spin–orbit (SO) effects, the GW approximation (G0W0), quantum confinement (QC), and polarization effects wherever applicable. (b) Optimized geometry of TTFDA molecules on PbS(001) surface (top-view). (c) Side-view of two PbS(001) cross-linked by a single TTFDA molecule in relaxed conformation.

excitonic binding energy and does not account for the electronic interactions between the two compounds. This correction is mainly made by the G_0W_0 term and is seen to result in a substantial increase of the gap in both PbS NCs and TTFDA. Therefore, the slightly larger gap energies compared to the spectroscopic data of the pure components seem reasonable. Our calculations predict a large energetic offset (>2 eV) between the $1S_e$ state and the LUMO as well as a near-resonant alignment ($\Delta E \approx 0.2$ eV) between the $1S_h$ state and the HOMO. In comparison to our previous work on the tetracarboxylate analogue, the expected resonance for the hole states is slightly weaker, which is also reflected in our CV data as discussed earlier.

We also display the geometric orientation of TTFDA on PbS(001) in top- (Figure 3b) and side-view (Figure 3c). Since there is only one binding site on each end of TTFDA, the binding mode to PbS(001) is markedly different from that of TTFDA, which bears two binding sites on each end.¹⁸ In effect, and since both molecules occupy roughly the same volume, the efficiency of surface passivation exerted by TTFDA on PbS(001) is expected to be smaller than for TTFDA. Also, the TTF-backbone, which stands out at an angle of almost 90° according to our computations for the tetracarboxylate, is now significantly tilted to a smaller angle due to the different binding mode in the dicarboxylate (Figure 3c).

In Figure 4, we examine the structural properties of PbS NCs exchanged with [TBA]₂TTFDA obtained with the liquid/air exchange by electron microscopy. We are particularly interested in NC periodicities due to self-assembly as well as any preferred directionality of such assembly. The former can be analyzed by an FFT of real-space micrographs, while the latter is obtained from selected area electron diffraction (SAED). Figure 4, panel a depicts the SAED of a circular area with 300 nm diameter of

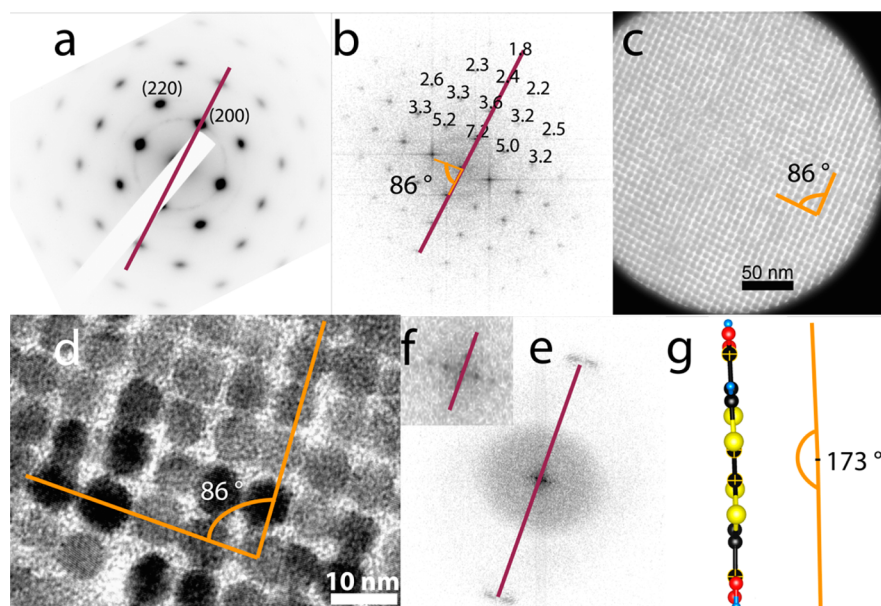


Figure 4. (a) SAED and (b) FFT of the real-space image in panel c. The SAED is indexed according to rock-salt PbS. All distances in the FFT are in nm^{-1} . The purple lines are parallel and serve as guidance to the eye. The tilt of the SAED was manually corrected with an external standard of known orientation. (d) Real space image of a PbS-TTFDA monolayer, (e) FFT thereof, and (f) zoom into the center of the FFT. Again, purple lines are parallel and serve as guidance to the eye. (g) Relaxed atomic positions and bonds of TTFDAH₂ according to DFT calculations and display of the dihedral angle of 173°.

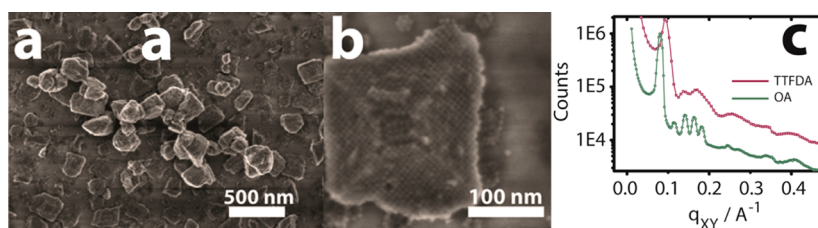


Figure 5. (a) Typical low magnification SEM micrograph of 5.0 (± 0.2) nm PbS-TTFDA and (b) high-magnification micrograph of a PbS-TTFDA supercrystal. (c) Grazing incidence X-ray diffraction (GIXD) of a large ensemble of the same PbS-TTFDA supercrystals (purple, TTFDA) and comparison with an ordered film of the same NCs capped with Pb[oleate]₂ (green, OA).

an NC film, the FFT, and real-space image of which are displayed in Figure 4, panels b and c. The practically single-crystalline pattern in Figure 4, panel a, which is consistent with the [001] zone axis of rock-salt PbS, indicates that each atomic lattice of all NCs within the spot is aligned in the same direction. Therefore, films of PbS-TTFDA fulfill the definition of a mesocrystal.¹⁹

From Figure 4, panel b, we infer that the NCs assemble in a quasi-cubic structure with a center-to-center distance of 7.2 nm. However, the structure is not precisely cubic, rather we consistently find an in-plane angle of 86 (± 1)° over several samples. To calculate the interparticle spacing, we measure the average length along the [001] direction of 200 NCs as 6.1 (± 0.4) nm (see Supporting Information, Figures S1b and S2b) and subtract it from the center-to-center distance. The interparticle spacing is therefore 1.1 nm, which is close to the nominal length of TTFDA (1.0 nm) and significantly shorter than typical values for Pb[oleate]₂ terminated NCs (1.8–2.4 nm).²⁹

We also investigate the structure of monolayered PbS-TTFDA (Figure 4d–f). We find the same in-plane angle of 86° (Figure 4d) and the same preferential orientation of atomic lattices along the [001] direction (Figure 4e). A magnification of the center of the FFT (Figure 4f) reveals that the NCs are

aligned uniaxially with the atomic lattices in the same way as in the multilayer example. Finally, the cartoon in Figure 4, panel g depicts the atomic structure with relaxed binding angles and distances of TTFDAH₂ according to our DFT calculations. We find that the dihedral angle, between terminal C atoms and the C=C bond in the center of the molecule, is 173°.

In Figure 5, panels a and b, we depict typical structures resulting from the solid/air ligand exchange applied to the NCs with the narrowest size-distribution in Table 1 ($d = 5.0 (\pm 0.2)$ nm). Rather than forming continuous films, these NCs

Table 1. Summary of the PbS NC Samples Utilized in This Work, Displaying the Mean NC Diameter, Its Standard Deviation (Both Inferred from TEM Micrographs), and the Maximum of the 1S_e ← 1S_h Transition (from Optical Absorption Spectroscopy)

nanoparticle diameter (nm)	standard deviation (nm)	first excitonic transition (meV)
5.0	0.2	760
6.3	1.0	722
7.5	1.2	686
8.8	1.0	613
9.7	1.0	564

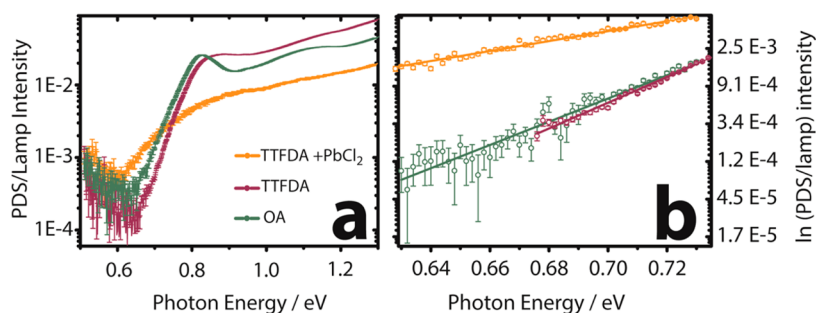


Figure 6. (a) PDS of PbS NCs with a first excitonic transition maximum at 0.83 eV and various surface functionalization: OA (green) = native ligand (Pb[oleate]₂), after ligand exchange with TTFDA (purple), and after TTFDA exchange followed by *c*-ALD with PbCl₂ (orange). Error bars are standard deviations of 20–1000 measurements per data point. (b) Urbach fits of all three samples (same color code applies) of the PDS/lamp signal against the photon energy in the vicinity of the 1S_e ← 1S_h transition.

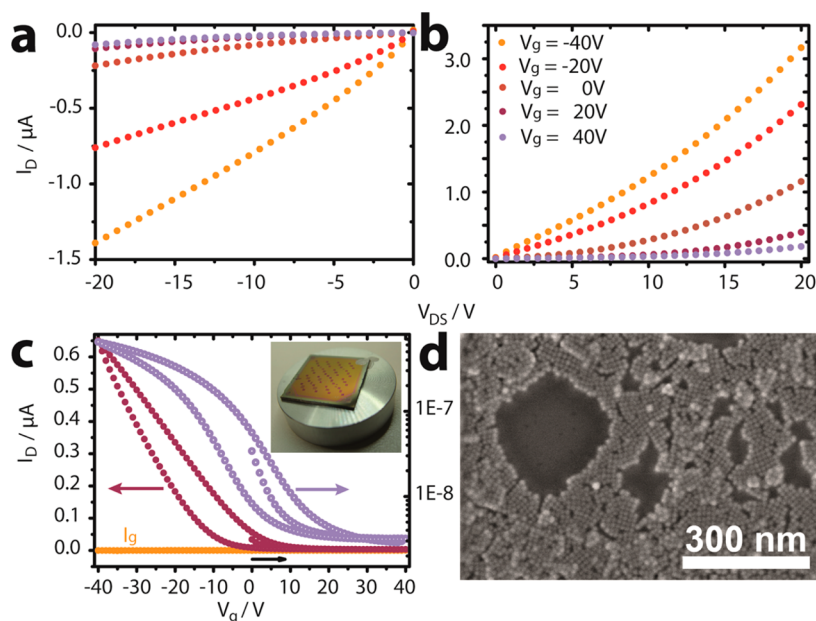


Figure 7. (a) Negative and (b) positive source–drain sweeps at the indicated gate voltages (V_G) of 9.7 (± 1.0) nm PbS–TTFDA thin films. (c) Transconductance at a constant bias of 5 V in linear and logarithmic presentation together with the gate leakage (I_g). The inset depicts a photograph of the device. (d) Typical SEM micrograph of part of a channel of the device after *c*-ALD with PbCl₂.

assemble spontaneously into three-dimensional supercrystals of TTFDA-functionalized PbS NCs. A similar behavior has been reported by Sigman et al. for dodecanethiol-capped Au NCs deposited from hexane solution, which was attributed to ligand–solvent interactions.²⁰ In contrast, we find that PbS NCs deposited from hexane before ligand exchange do not typically show this assembly behavior, suggesting that the ligand exchange and the resulting volume contraction as well as cross-linkage are important driving forces in the assembly. Upon exchange with TTFDA of all other NC samples (with wider size distribution), the formation of continuous films is favored over that of supercrystals (see Figure 7d).

We monitor the volume contraction during ligand exchange with TTFDA by grazing incidence X-ray diffraction (GIXD) (Figure 5c). While both patterns resemble a similar structure, after ligand exchange, all reflections are shifted toward higher q -values, indicating a smaller unit cell and shorter interparticle spacing. The first prominent reflection, for instance, is shifted from 0.080 Å⁻¹ to 0.092 Å⁻¹, translating into a real-space contraction of 1.0 nm. Further, as can be seen particularly in the q -range 0.1–0.2 Å⁻¹, all reflections appear to broaden slightly,

indicating a certain loss of structural coherence during ligand exchange. While a full quantitative analysis of the structural coherence and sources of disorder is beyond the scope of the present paper, we can provide estimates of the average coherence lengths. We find typical peak widths (fwhm) of $\Delta q = 0.012$ Å⁻¹ (corresponding to about 54 nm, i.e., ~10 particles) before and $\Delta q = 0.018$ Å⁻¹ (corresponding to about 34 nm, i.e., ~7 particles) after ligand exchange. We note, though, that the domains with the highest degree of order will exhibit substantially longer coherence lengths than these average numbers. Further, cumulative disorder due to the inherent size-distribution of NCs is known to complicate the relationship between coherence length and grain size.²¹

While conventional optical spectroscopy is typically not sensitive enough to detect transitions involving trap states, in Figure 6, panel a we use the extraordinary sensitivity of photothermal deflection spectroscopy (PDS) to investigate optical transitions between 0.5 eV and the 1S_e ← 1S_h transition. For PbS NCs with a 1S_e ← 1S_h maximum of 0.83 eV and native ligand (Pb[oleate]₂), we find moderate tailing and an absorption onset at 0.65 eV. After ligand exchange with

TTFDA, the absorption onset is still positioned at 0.65 eV, but the $1S_e \leftarrow 1S_h$ maximum has undergone a hypsochromic shift toward ~ 0.86 eV. Following the model by Urbach, in Figure 6, panel b, we fit the absorption tails as $\exp(E/E_U)$, with the phonon energy E and the characteristic Urbach energy E_U .²² We observe a small decrease in E_U when exchanging the native ligand ($E_U = 34$ meV) with TTFDA ($E_U = 29$ meV).

We also carry out optical absorption spectroscopy in transmission of thin films of all samples in Table 1 to investigate shifts in the $1S_e \leftarrow 1S_h$ transition. In agreement with the PDS data, we typically detect moderate hypsochromic shifts for PbS NCs with larger bandgaps (760 and 722 meV) and small bathochromic shifts for the NCs with the smallest bandgap (564 meV, see Figure S3 in the Supporting Information), but no robust trends could be established. Our preliminary photoluminescence (PL) studies of PbS NCs capped with TTFDA using a Germanium detector with cutoff below 0.77 eV at 300 K indicate that small particles (4.2 nm, Figure S4 in the Supporting Information) exhibit strong PL with largely unchanged peak positions and full width at half maxima as compared to the same NCs capped with Pb[oleate]₂. In contrast, the PL signal of larger NCs (7.5 nm, data not shown) is quenched upon ligand exchange from Pb[oleate]₂ to TTFDA.

Oh et al. have demonstrated that films of PbS NCs undergo strong n-type doping when treated with a warm solution of PbCl₂ dissolved in oleylamine.⁴⁴ Such colloidal atomic layer deposition (c-ALD) changes the stoichiometry of the NC surfaces toward a Pb-rich environment, which presumably creates filled in-gap states close to the $1S_e$ level. To test this hypothesis, we apply c-ALD with PbCl₂ to the same PbS NCs capped with TTFDA and measure PDS (Figure 6a). The absorption onset is red-shifted to 0.61 eV and the $1S_e \leftarrow 1S_h$ transition substantially broadened with a relative maximum around 0.86 eV and strong tailing into the bandgap. The corresponding Urbach plot is presented in Figure 6, panel b, revealing a large Urbach energy of 76 meV. As verified by SEM, the size distribution of the NCs remains unchanged after treatment with PbCl₂. We note that previously brightly luminescent PbS NCs capped with TTFDA are entirely quenched upon c-ALD with PbCl₂.

To investigate the degree of electronic coupling in PbS-TTFDA, we use the field-effect mobility as an easily accessible measure for the efficiency of carrier transport. Field-effect transistors are fabricated on Si/SiO_x bottom-gate, bottom-contact substrates by spin-coating PbS NCs and subsequent exchange with [TBA]₂TTFDA at the solid/air interface. Typical I/V -curves at varying gate bias (V_G) are displayed in Figure 7, both for negative (Figure 7a) and positive source-drain voltage (V_{DS} , Figure 7b). While pinch-off is not reached in these devices at reasonable V_{DS} (presumably due to a relatively high carrier concentration), the film is clearly hole-conducting. The transconductance (Figure 7c) at $V_{DS} = 5$ V for a full cycle of $V_G = 0 \text{ V} \rightarrow +40 \text{ V} \rightarrow -40 \text{ V} \rightarrow 0 \text{ V}$ shows moderate hysteresis, which is commonly observed in PbS NC transistors and often attributed to electron trapping at the SiO_x/PbS interface. To extract the field-effect mobilities via the gradual channel approximation, we assume that charge transport will predominantly take place within the bottom single layer and apply a correction method to account for the voids in the film to obtain an effective channel width (W). For details, see the Supporting Information.

For the largest NCs ($d = 9.7$ nm) we find mobilities of up to 1×10^{-4} cm²/(V s). We note that mobilities extracted from FET measurements are effective mobilities, which are prone to contact resistances, injection barriers, recombinations, etc. such that they do not necessarily reflect the real, intrinsic mobilities. Further, the choice of device architecture, such as bottom-gate, bottom-contact versus top-gate, bottom-contact, different gate dielectrics, or metal contacts can greatly influence the magnitude of the effective mobilities.^{23,24} Nonetheless, for the comparison of similar materials, FET mobilities provide a good starting point. In this respect, we have also measured the transconductance of 6.3 nm PbS NCs after ligand exchange with 1,2-ethanedithiol (EDT, Figure S5 in the Supporting Information). In contrast to the unipolar transport of the same NCs capped with TTFDA, here we find ambipolar behavior, which is consistent with previous reports. An average field-effect hole mobility of 4×10^{-6} cm²/(V s) and a carrier concentration of 1.1×10^{16} cm⁻³ are not substantially different from the values obtained for TTFDA functionalization. Osedach et al. have previously investigated EDT-capped PbS NCs of sizes between 2.9 and 6.8 nm and reported field-effect hole mobilities of 3×10^{-3} cm²/(V s) using various dielectrics in a bottom-contact, top-gate geometry.⁵⁴

Figure 7, panel d depicts the morphology of a typical NC transistor channel. The film is mostly monolayered with a substantial portion of voids. While these voids can be filled-in to grow thicker films, we generally find that this leads to poorly defined NC packing such that we avoid it intentionally. For a single monolayer, the packing is predominantly cubic, at least on short-range.

In Figure 8, panel a, we explore the effect of the size-dependent field-effect mobilities of the NCs with diameters and

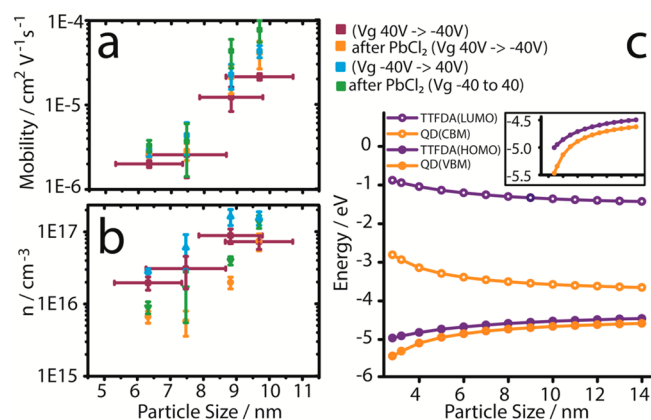


Figure 8. (a) Size-dependent field-effect hole mobilities of PbS-TTFDA thin films before and after c-ALD with PbCl₂ and in the scan direction of the transconductance as indicated in the figure legend. (b) Hole concentrations inferred from the field-effect mobilities according to Ohm's law. Vertical error bars are standard deviations over 16 measurements. (c) Calculated size-dependence of the absolute positions of the $1S_h$ and $1S_e$ state of PbS NCs as well as the HOMO and LUMO of TTFDA after surface functionalization. The inset is a zoom into the size-dependent HOMO- $1S_h$ offset.

size-distribution listed in Table 1. The horizontal error bars reflect the size-distributions (exemplarily shown for one measurement set only), while the vertical error bars are the standard deviations over 16 measurements (for details on the error analysis, see the Supporting Information). We were unable to fabricate thin, continuous films of the 5.0 (± 0.2) nm

NCs, as shown in Figure 5, such that the transport properties of these NCs could not be assessed. As-exchanged PbS–TTFDA films are denoted in purple or turquoise, depending on the V_g scan direction. The differences in the extracted mobilities for both scan directions are a consequence of the hysteresis already described in Figure 7, panel c. Since the field-effect mobility is an effective mobility, which includes the effect of traps, we also investigate how the mobility changes upon improving the NC surface passivation.⁴⁹ For PbS NCs, this is conveniently achieved by the same c-ALD procedure as introduced around Figure 6, panel b.⁴⁴ Mobilities after c-ALD are represented in orange or green in Figure 8, panel a, again depending on the scan direction. In general, the mobilities increase with respect to the untreated samples (by $\leq 50\%$). The field-effect mobilities range between $2 \times 10^{-6} \text{ cm}^2/(\text{V s})$ for 6.3 nm PbS and $8 \times 10^{-5} \text{ cm}^2/(\text{V s})$ for 9.7 nm PbS NCs.

The effect of PbCl_2 treatment is also apparent in the extracted carrier concentrations in Figure 8, panel b. For untreated NCs, the general size-effect observed is an increase from $2 \times 10^{16} \text{ cm}^{-3}$ for the smallest NCs to $1 \times 10^{17} \text{ cm}^{-3}$ for the largest NCs. After PbCl_2 treatment, all carrier concentrations are observed to be lower with $8 \times 10^{15} \text{ cm}^{-3}$ for the smallest and $9 \times 10^{16} \text{ cm}^{-3}$ for the largest NCs.

To understand these results in more detail, we use DFT to calculate the $1S_c/\text{LUMO}$ and $1S_h/\text{HOMO}$ energetic alignment as a function of the PbS NC diameter in Figure 8, panel c. As expected, the $1S_h/\text{HOMO}$ offset decreases with increasing diameter toward approximately 0.2 eV for large diameters (see also the inset of Figure 8c), while the $1S_c/\text{LUMO}$ offset is large over the entire range of NC diameters. In addition, the HOMO–LUMO gap of TTFDA bound to the surface of PbS NCs decreases also with increasing diameter. This is predominantly a consequence of a change in the polarization exerted onto TTFDA by PbS NCs of varying sizes.

DISCUSSION

The tendency of PbS NCs to assemble into mesocrystals (Figure 4) upon cross-linkage with TTFDA is a unique advantage over other ligand exchange strategies, particularly those operating with very short molecules. Our data imply that TTFDA strongly favors binding to PbS(001) and that the structural rigidity of the π -system invokes a static interparticle distance onto the NC lattice. Such structural rigidity is typically not encountered for PbS NCs functionalized with sp^3 -hybridized, monodentate ligands (such as $\text{Pb}[\text{oleate}]_2$), where variations in the interparticle spacing and the orientation of atomic lattices within the NC lattice are frequently observed.^{25–29} The occurrence of the same iso-oriented structure in a single NC monolayer (Figure 4d–f) supports our view of TTFDA as a rigid cross-linker, which directs the NCs into the displayed structure by strong in-plane interactions. This is remarkable since PbS NCs functionalized with $\text{Pb}[\text{oleate}]_2$ typically display poor directionality on the monolayer level even if the corresponding multilayer is truly mesocrystalline. We therefore conclude that for $[\text{Pb}]\text{TTFDA}$ functionalization, the in-plane ligand interactions are already strong enough to induce directional assembly. In terms of the deviation from a truly cubic lattice (86° vs 90°) for the PbS–TTFDA mesocrystals (Figure 4b–d), we speculate that the dihedral angle of 173° in TTFDA (Figure 4g) may play a role here. This angle could result in a relative displacement between the two axes of symmetry of connected NCs resulting in a

($180^\circ - 173^\circ/2$) deviation from ideal cubic packing, as observed in experiment.

The spontaneous assembly into 3D-mesocrystals of the 5.0 (± 0.2) nm PbS crystals upon solid/air exchange with TTFDA (Figure 5) is another indication of the directional force exerted by TTFDA on PbS NC ensembles. Typically, such assemblies are obtained from samples of narrow size-distribution by slow (\sim several weeks), polarity-gradient driven crystallization in solution, as for instance demonstrated for $\text{Pb}[\text{oleate}]_2$ -capped PbS NCs.³⁰ In the present work, the crystallization occurs within few seconds and in a single solvent, such that the crystallization mechanism is markedly different. We assume that the directional cross-linkage with TTFDA is primarily responsible for the crystallization. We speculate that for the other PbS NC samples, crystallization does not occur under these conditions because of the relatively small lattice enthalpy released in the periodic assembly of inhomogeneous NC ensembles.

Our GIXD data (Figure 5c) confirm that the high degree of local order in PbS–TTFDA mesocrystals examined by electron microscopy is also observed on a macroscopic length scale over several millimeters.

The PDS data (Figure 6) indicate that TTFDA functionalization leads to a broadened $1S_c \leftarrow 1S_h$ transition and a slightly reduced disorder of the electronic structure close to the $1S_c/1S_h$ edges compared to $\text{Pb}[\text{oleate}]_2$ -capping. Disorder leading to Urbach tails can have a variety of origins such as strain, compositional fluctuations, and also defects.^{31,32,35} For silicon, Urbach energies typically vary between 10 meV for high-quality, single-crystal Si and >50 meV for amorphous Si.³³ For high-quality CdSe and PbSe NCs, Urbach energies of ~ 23 meV have been reported.^{34,35} By using intensity correlated photocurrent spectroscopy, Urbach energies between 13–15 meV were found for PbS NCs capped with EDT.³⁶ In this light, the slightly higher values measured in this work for TTFDA passivation (29 meV) support the extracted free carrier concentrations (Figure 8b) and the view of PbS–TTFDA as a moderately doped, yet well-passivated quantum dot solid. In contrast, the fact that the Urbach energy increases profoundly after c-ALD with PbCl_2 (“TTFDA + PbCl_2 ”, 76 meV) provides supporting evidence for the introduction of a large density of defect states, probably by excess lead at the surface as reported by Oh et al.⁴⁴

These findings are supported by our PL measurements of the same PbS NCs as those analyzed in Figure 6, panel a, which reveal largely preserved luminescence after TTFDA functionalization and complete quenching of the PL after c-ALD with PbCl_2 .

Optical absorption spectroscopy before and after ligand exchange is often applied to monitor dipole–dipole interactions as well as electronic coupling in NC ensembles. When the interparticle distance between adjacent NCs shrinks, a bathochromic shift of the $1S_c \leftarrow 1S_h$ transition is often observed, the origin of which has been discussed controversially, particularly for PbSe NCs.^{37–39,48} Generally, the bathochromic shift can originate from both increased electronic coupling due to an increased transmission coefficient as well as transition dipole coupling due to decreased dielectric screening of excitons. For 1,2-ethanedithiol functionalized PbS NCs, bathochromic shifts of the $1S_c \leftarrow 1S_h$ transition by ~ 80 meV have been reported, and for S^{2-} treated PbS NCs, the shift was ~ 100 meV.^{40,44} The transition dipole coupling energy (E_{Dipole}) is given by

$$E_{\text{Dipole}} = \frac{\mu_{\text{tr}}^2 \alpha}{\pi \epsilon_0} D^{-6}$$

where μ_{tr} is the transition dipole moment, α the polarizability volume, ϵ_0 the vacuum permittivity, and D the interparticle spacing.⁴¹ Since μ_{tr} is largely constant for the same NC sample, and the change in α is small unless drastic differences in the dielectric constants of the interchanged ligands exist, E_{Dipole} is first and foremost a function of the interparticle distance. However, the barely existent bathochromic shift after exchange with TTFDA for large PbS NCs (Figure S3) and the even hypsochromic shift for smaller PbS NCs (Figure 6a) indicate a somewhat more complex origin of the optical shifts. As established by GIXD (Figure 5c), ΔD , although smaller than for EDT or S^{2-} -capping, is still negative upon ligand exchange such that bathochromic shifts are expected for all samples. In this situation, a smaller effective dielectric constant after ligand exchange is the most likely explanation for a hypsochromic shift. (Note that great care was taken to prevent oxidation of all samples and that Cl^- -terminated PbS NCs tend to have robust optical absorption properties even after long-term exposure to air.)

A central hypothesis in the concept of COINs is the tunability of interparticle electronic coupling via the energetic position of relevant states of the NC.⁴² If the 1S_c state is in close energetic proximity to the LUMO of the OSC, a channel for electron transport can form, while a resonance between the 1S_h state and the HOMO can lead to efficient coupling of holes. Because of the quantum size effect in semiconductor NCs, these resonances may be tuned via the NC size. As already established for 10 nm PbS NCs by DFT in Figure 3, panel a, the 1S_c -LUMO offset is large compared to the 1S_h -HOMO offset such that hole transport should be favored over electron transport. This is in accordance with the unipolar hole transport displayed in Figure 7, but since such transport characteristics could also be the result of other factors, such as surface vacancies, a more detailed discussion is required.⁴³ First, we can rule out that electron transport in the NCs used in this study is generally suppressed by surface defects or an oxidative environment during transport measurements in light of the ambipolar transport characteristics observed upon EDT functionalization (Figure S5). To further elucidate the origin of unipolar transport for TTFDA capping, the results of the c-ALD after ligand exchange (Figure 8a,b) are instructive. In the original paper by Oh et al., c-ALD rapidly decreases the hole concentration in degenerately doped PbS NCs by removing Pb-vacancies on the surface and drives the system through an ambipolar state into n-type within 10 min.⁴⁴ For TTFDA-functionalized PbS NCs, we have established by PDS (Figure 6b) that the density of states within the 1S_h - 1S_c gap is indeed profoundly altered during c-ALD. In addition, the complete quenching of PL resulting from this treatments also indicates the evolution of a large number of surface states, which, according to Oh et al., should lead to n-type doping. However, the material remains p-type even after prolonged exposure to PbCl_2 ; the hole concentration decreases slightly, and the hole mobility exhibits a moderate increase (compare Figure 8a,b). This indicates that the origin of hole conduction is different from that in PbS NCs exchanged with S^{2-} or EDT for instance. We believe that the energetic proximity of the NC 1S_h state and the HOMO of TTFDA is responsible for the unipolar hole transport. In such a scenario, the surface stoichiometry of the NCs has only limited influence onto the predominant carrier

type because holes are much more efficiently transmitted through the NC film than electrons.

Osedach et al. have found that the field-effect hole mobilities for EDT-capped PbS NCs increase dramatically with size until ~ 4.4 nm, after which they remain practically invariant with the diameter within the studied regime (6.8 nm max). In contrast, the mobilities of TTFDA-functionalized PbS NCs (Figure 8a) are strongly size-dependent and follow the predicted trend of Figure 8, panel c, which could be interpreted with energy level tuning of the 1S_h -HOMO offset via the quantum size effect. In principal, one would expect an exponential increase with a linearly decreasing 1S_h -HOMO offset, which is reflected by our data (Figure 8a). It is worthwhile to note that Zhang et al. have recently shown how PL quantum yield measurements can be used to quantify electronic coupling in NC ensembles.⁴⁵ Briefly, enhanced coupling provides additional pathways for non-radiative carrier recombination and decreases the PL quantum yield. Therefore, our observation that small PbS-TTFDA particle films are luminescent, whereas films comprising of larger NCs are not, is also supportive of increased coupling with increasing NC diameter in this material. On the other hand, the size-dependent optoelectronic properties of NCs are rather complex. Semonin et al. have shown that the PL quantum yield of PbS NCs functionalized with oleic acid drops dramatically with increasing the NC diameter.⁴⁶ For PbSe NCs, Liu et al. report a four-fold increase for the hole mobilities in the range of 6–10 nm, while with a slightly different surface functionalization, the mobility can even drop by over an order of magnitude.^{47,48} Yazdani et al. use time-of-flight measurements to study the intrinsic (not effective) mobility of PbS NCs in the range of 2.4–4.8 nm and find a 20-fold decrease of the mobility with increasing size.⁴⁹ Therefore, the size-dependent PL quenching and the effective mobilities in the present work need to be interpreted with care and would require further investigations to unambiguously prove that transport is dominated by the 1S_h -HOMO offset. Here, in situ conductance measurements under electrochemical gating could be helpful to investigate the mobility of holes injected into the 1S_h state.⁵⁰ Also, an assessment of the intrinsic mobilities by contactless transport measurement techniques, such as time-resolved microwave conductance or Terahertz spectroscopy, should be considered in the future.^{51–53} In this regard, detailed knowledge about typical excitonic lifetimes would be beneficial, which may be extracted from transient absorption or time-resolved PL measurements. Nevertheless, the detected modulation of the mobility is quite remarkable, particularly in view of the relatively poor energy level alignment displayed in Figure 8, panel c. We stress that the potential of COINs, such as the PbS-TTFDA material presented here, should not be solely evaluated by simply judging the field-effect mobilities. In fact, the large discrepancy in the magnitude of the hole mobility for EDT-capped PbS NCs obtained by Osedach et al. versus that measured by us (using a rather simple bottom-gate, bottom-contact device architecture) underlines that optimizing the device geometry is mandatory to compete with other state-of-the-art examples of NCs treated by a short-ligand-exchange of choice.⁵⁴ Rather, it is the perspective to form conductive mesocrystals with the potential to allow for direction-dependent transport, which renders this system an interesting and under-explored alternative for the design of NC-based optoelectronic materials. Future studies will have to assess to which extent the effective mobilities can be optimized, for instance by considering different device architectures as already

discussed. In addition, changes to the design of the surface molecule should be considered to lower the position of the HOMO and facilitate the occurrence of a resonance with the PbS $1S_h$ state, also for smaller NC diameter, which would be particularly relevant for photovoltaic applications. This could be achieved, for example, by using the TTF derivative tetrathiafulvalene tetrabenzoate and introducing electron-withdrawing substituents to the phenyl rings.⁵⁵

CONCLUSION

We have demonstrated that TTFDA serves as a rigid and directional cross-linker for PbS nanocrystals leading to the spontaneous assembly into conductive mesocrystals. Presumably due to near resonant alignment between the PbS $1S_h$ state and the HOMO of TTFDA, these mesocrystalline assemblies are unipolar and hole-conducting, and the carrier mobilities can be tuned via the nanocrystal diameter. The transport mode is robust against surface modifications, which typically lead to n-type transport, indicating that an inherent preference for hole transport is indeed present in the material. Future linker molecules to fabricate conductive PbS mesocrystals should contain a HOMO situated significantly lower than that of TTFDA to optimize the resonance via the PbS diameter. Because of the smaller effective mass of electrons, π -systems with LUMO positions suitable for coupling to the PbS $1S_c$ state should also be considered.

METHODS

Synthesis of PbS Nanocrystals. The PbS NC samples were synthesized by a previously reported method.⁵⁶ The NCs were precipitated by the addition of anhydrous ethanol, the suspension centrifuged for 5 min at 4500 rpm, the supernatant discarded, and the precipitate dissolved in anhydrous hexanes. It was washed two more times on adding anhydrous ethanol and one more time with acetone. The NCs were stored in anhydrous hexanes.

Synthesis of $[TBA]_2TTFDA$. The neutral TTF dicarboxylic acid was synthesized as previously described.⁵⁷ The neutral diacid (1.0 g, 3.4 mmol, 1 equiv) was suspended in anhydrous MeOH (30 mL), to which tetrabutylammonium hydroxide (6.8 mL, 1.0 M solution in MeOH, 2 equiv) was added. The resulting mixture was stirred at room temperature for 2 h, followed by filtration to remove the partially deprotonated TTF salts. The volume of the remaining filtrate was concentrated to 3 mL. Upon addition of ethyl ether (~100 mL), an oily precipitate was obtained, which was rinsed thoroughly with ether to give $[TBA]_2TTFDA$ (1.77 g, 67% yield) as an orange semisolid.

Ligand Exchange with TTFDA—Solid/Air Exchange. Three milligrams of $[TBA]_2TTFDA$ was dissolved with 3 mL of methanol. Substrates for various characterization methods (FET, XPS, PDS, SEM, GIXD, etc.) were cleaned on using soap scrub, rinsed with distilled water, followed by isopropanol and acetone, blow-dried, UV/ozone cleaned for 5 min, and mounted onto a spin-coater. One drop of a filtered hexanes solution of nanoparticles (roughly 1 mg/mL) was drop-cast onto the substrate and spun at 2000 rpm with a 1 s ramp for 15 s. At rest, the substrate was covered with the TTFDA solution (approximately 200 μ L) and allowed to dry completely within roughly 10 min. While spinning at 2000 rpm, it was washed with methanol to spin-off excess TTFDA followed by hexanes to wash off the oleate. This procedure was repeated one more time to yield a continuous film.

Ligand Exchange with TTFDA—Liquid/Air Exchange. Three milligrams of $[TBA]_2TTFDA$ was dissolved with 3 mL of methanol in a Teflon well. Two-hundred microliters of a dilute solution of PbS nanocrystals in hexane (~0.1 mg/mL) was carefully deposited on top of the methanol solution and allowed to dry under a glass slide cover. The barely visible, floating membrane of NCs that formed on top of the methanolic TTFDA solution was allowed to ligand exchange and assemble overnight.

The TTFDA-exchanged membrane was carefully “stamped” onto a desired support (Si substrate or Cu/C grid) by holding the substrate upside-down and approaching the membrane from the top. The transferred membrane was mildly annealed at 80 °C for 20 min and the film carefully rinsed with methanol to remove excess TTFDA.

ASSOCIATED CONTENT

Supporting Information

The Supporting Information is available free of charge on the ACS Publications website at DOI: [10.1021/acs.chemmater.5b03821](https://doi.org/10.1021/acs.chemmater.5b03821).

Statistical analysis and electron microscopy micrographs of the PbS nanocrystal samples used in this work; optical absorption spectrum of an optically thick film of 9.7 (± 1.0) nm PbS NCs before and after ligand exchange with TTFDA; normalized photoluminescence of PbS NCs before and after exchange with TTFDA; transconductance of 6.3 nm PbS NCs exchanged with 1,2-ethanedithiol; calculated atomic structure, total charge density, and HOMO and LUMO wave functions of a cuboctahedral PbS nanoparticle; calculated HOMO and LUMO charge densities of TTFDA; description of characterization techniques, the correction method applied to account for voids in the particle film, the error analysis for FET measurements, and theoretical calculations (PDF)

AUTHOR INFORMATION

Corresponding Author

*E-mail: marcus.scheele@uni.tuebingen.de.

Author Contributions

The manuscript was written through contributions of all authors. All authors have given approval to the final version of the manuscript.

Notes

The authors declare no competing financial interest.

ACKNOWLEDGMENTS

Financial support of A.A., M.S.K., and M.S. has been provided in equal parts by the Institutional Strategy of the University of Tübingen (Deutsche Forschungsgemeinschaft, ZUK 63) and the Baden-Württemberg Stiftung by the Eliteprogram for Postdocs. Y.L. and B.H. acknowledge the support from the Self-Assembly of Organic/Inorganic Nanocomposite Materials program, and the synthesis of TTFDA and optical spectroscopy were performed as a User Project at the Molecular Foundry, Lawrence Berkeley National Laboratory, all supported by the Office of Science, Office of Basic Energy Sciences, U.S. Department of Energy, under Contract No. DE-AC02-05CH11231. D.H. was supported in part by an award from The Paul and Daisy Soros Fellowship for New Americans and NSF-GFRP. We are grateful to Horst Weller for allowance to use a JEM-Jeol-1011 microscope. Rupak Banerjee and Jiri Novak are acknowledged for help with the GIXD measurements. PDS experiments were partially supported by the Ministry for Science, Research, and the Arts, Baden-Württemberg.

REFERENCES

(1) Zhang, H.; Jang, J.; Liu, W.; Talapin, D. V. Colloidal Nanocrystals with Inorganic Halide, Pseudohalide, and Halometallate Ligands. *ACS Nano* 2014, 8, 7359–7369.

- (2) Dong, A.; Jiao, Y.; Milliron, D. J. Electronically Coupled Nanocrystal Superlattice Films by in Situ Ligand Exchange at the Liquid-Air Interface. *ACS Nano* **2013**, *7*, 10978–10984.
- (3) Bahrig, L.; Hickey, S. G.; Eychmüller, A. Mesocrystalline Materials and the Involvement of Oriented Attachment - a Review. *CrystEngComm* **2014**, *16*, 9408–9424.
- (4) Boneschanscher, M. P.; Evers, W. H.; Geuchies, J. J.; Altantzis, T.; Goris, B.; Rabouw, F. T.; van Rossum, S. A. P.; van der Zant, H. S. J.; Siebbeles, L. D. A.; Van Tendeloo, G.; et al. Long-range Orientation and Atomic Attachment of Nanocrystals in 2D Honeycomb Superlattices. *Science* **2014**, *344*, 1377–1380.
- (5) Murray, C. B.; Kagan, C. R.; Bawendi, M. G. Self-Organization of CdSe Nanocrystallites into Three-Dimensional Quantum Dot Superlattices. *Science* **1995**, *270*, 1335–1338.
- (6) Kaushik, A. P.; Lukose, B.; Clancy, P. The Role of Shape on Electronic Structure and Charge Transport in Faceted PbSe Nanocrystals. *ACS Nano* **2014**, *8*, 2302–2317.
- (7) Weidman, M. C.; Yager, K. G.; Tisdale, W. A. Interparticle Spacing and Structural Ordering in Superlattice PbS Nanocrystal Solids Undergoing Ligand Exchange. *Chem. Mater.* **2015**, *27*, 474–482.
- (8) Moreels, I.; Justo, Y.; De Geyter, B.; Haustraete, K.; Martins, J. C.; Hens, Z. Size-Tunable, Bright, and Stable PbS Quantum Dots: A Surface Chemistry Study. *ACS Nano* **2011**, *5*, 2004–2012.
- (9) Zherebetskyy, D.; Scheele, M.; Zhang, Y.; Bronstein, N.; Thompson, C.; Britt, D.; Salmeron, M.; Alivisatos, P.; Wang, L.-W. Hydroxylation of the Surface of PbS Nanocrystals Passivated with Oleic Acid. *Science* **2014**, *344*, 1380–1384.
- (10) Mercier, N.; Giffard, M.; Pilet, G.; Allain, M.; Hudhomme, P.; Mabon, G.; Levillain, E.; Gorgues, A.; Riou, A. (TTF)₂[TTF-(CO₂H)₂(CO₂)₂]: a Wholly TTF Material Containing TTF Radical Cations and TTF Derived Anions. *Chem. Commun.* **2001**, 2722–2723.
- (11) Cardona, C. M.; Li, W.; Kaifer, A. E.; Stockdale, D.; Bazan, G. C. Electrochemical Considerations for Determining Absolute Frontier Orbital Energy Levels of Conjugated Polymers for Solar Cell Applications. *Adv. Mater.* **2011**, *23*, 2367–2371.
- (12) Hintz, H.; Peisert, H.; Egelhaaf, H.-J.; Chassé, T. Reversible and Irreversible Light-Induced p-Doping of P3HT by Oxygen Studied by Photoelectron Spectroscopy (XPS/UPS). *J. Phys. Chem. C* **2011**, *115*, 13373–13376.
- (13) Preobrajenski, A.; Chassé, T. Epitaxial Growth and Interface Structure of PbS on InP(110). *Appl. Surf. Sci.* **1999**, *142*, 394–399.
- (14) Moreels, I.; Fritzing, B.; Martins, J. C.; Hens, Z. Surface Chemistry of Colloidal PbSe Nanocrystals. *J. Am. Chem. Soc.* **2008**, *130*, 15081–15086.
- (15) Axnanda, S.; Scheele, M.; Crumlin, E.; Mao, B.; Chang, R.; Rani, S.; Faiz, M.; Wang, S.; Alivisatos, A. P.; Liu, Z. Direct Work Function Measurement by Gas Phase Photoelectron Spectroscopy and Its Application on PbS Nanoparticles. *Nano Lett.* **2013**, *13*, 6176–6182.
- (16) Brown, P. R.; Kim, D.; Lunt, R. R.; Zhao, N.; Bawendi, M. G.; Grossman, J. C.; Bulovic, V. Energy Level Modification in Lead Sulfide Quantum Dot Thin Films through Ligand Exchange. *ACS Nano* **2014**, *8*, 5863–5872.
- (17) Jasieniak, J.; Califano, M.; Watkins, S. E. Size-Dependent Valence and Conduction Band-Edge Energies of Semiconductor Nanocrystals. *ACS Nano* **2011**, *5*, 5888–5902.
- (18) Scheele, M.; Hanifi, D.; Zherebetskyy, D.; Chourou, S. T.; Axnanda, S.; Rancatore, B. J.; Thorkelsson, K.; Xu, T.; Liu, Z.; Wang, L.-W.; et al. PbS Nanoparticles Capped with Tetrathiafulvalenetracarboxylate: Utilizing Energy Level Alignment for Efficient Carrier Transport. *ACS Nano* **2014**, *8*, 2532–2540.
- (19) Cölfen, H.; Antonietti, M. Mesocrystals: Inorganic Superstructures Made by Highly Parallel Crystallization and Controlled Alignment. *Angew. Chem., Int. Ed.* **2005**, *44*, 5576–5591.
- (20) Sigman, M. B.; Saunders, A. E.; Korgel, B. A. Metal Nanocrystal Superlattice Nucleation and Growth. *Langmuir* **2004**, *20*, 978–983.
- (21) Rivnay, J.; Mannsfeld, S. C. B.; Miller, C. E.; Salleo, A.; Toney, M. F. Quantitative Determination of Organic Semiconductor Microstructure from the Molecular to Device Scale. *Chem. Rev.* **2012**, *112*, 5488–5519.
- (22) Urbach, F. The Long-Wavelength Edge of Photographic Sensitivity and of the Electronic Absorption of Solids. *Phys. Rev.* **1953**, *92*, 1324–1324.
- (23) Bisri, S. Z.; Piliago, C.; Yarema, M.; Heiss, W.; Loi, M. A. Low Driving Voltage and High Mobility Ambipolar Field-Effect Transistors with PbS Colloidal Nanocrystals. *Adv. Mater.* **2013**, *25*, 4309–4314.
- (24) Klauk, H. Organic Thin-film Transistors. *Chem. Soc. Rev.* **2010**, *39*, 2643–2666.
- (25) Bian, K.; Choi, J. J.; Kaushik, A.; Clancy, P.; Smilgies, D.-M.; Hanrath, T. Shape-Anisotropy Driven Symmetry Transformations in Nanocrystal Superlattice Polymorphs. *ACS Nano* **2011**, *5*, 2815–2823.
- (26) Choi, J. J.; Bealing, C. R.; Bian, K.; Hughes, K. J.; Zhang, W.; Smilgies, D.-M.; Hennig, R. G.; Engstrom, J. R.; Hanrath, T. Controlling Nanocrystal Superlattice Symmetry and Shape-Anisotropic Interactions through Variable Ligand Surface Coverage. *J. Am. Chem. Soc.* **2011**, *133*, 3131–3138.
- (27) Li, R.; Bian, K.; Hanrath, T.; Bassett, W. A.; Wang, Z. Decoding the Superlattice and Interface Structure of Truncate PbS Nanocrystal-Assembled Supercrystal and Associated Interaction Forces. *J. Am. Chem. Soc.* **2014**, *136*, 12047–12055.
- (28) Simon, P.; Rosseeva, E.; Baburin, I. A.; Liebscher, L.; Hickey, S. G.; Cardoso-Gil, R.; Eychmüller, A.; Kniep, R.; Carrillo-Cabrera, W. PbS-Organic Mesocrystals: The Relationship Between Nanocrystal Orientation and Superlattice Array. *Angew. Chem., Int. Ed.* **2012**, *51*, 10776–10781.
- (29) Wang, Z.; Schliehe, C.; Bian, K.; Dale, D.; Bassett, W. A.; Hanrath, T.; Klinke, C.; Weller, H. Correlating Superlattice Polymorphs to Internanoparticle Distance, Packing Density, and Surface Lattice in Assemblies of PbS Nanoparticles. *Nano Lett.* **2013**, *13*, 1303–1311.
- (30) Nagel, M.; Hickey, S. G.; Frömsdorf, A.; Kornowski, A.; Weller, H. Synthesis of Monodisperse PbS Nanoparticles and Their Assembly into Highly Ordered 3D Colloidal Crystals. *Z. Phys. Chem.* **2007**, *221*, 427–437.
- (31) Cody, G. D. Urbach Edge of Crystalline and Amorphous Silicon: a Personal Review. *J. Non-Cryst. Solids* **1992**, *141*, 3–15.
- (32) Skumanich, A.; Frova, A.; Amer, N. M. Urbach Tail and Gap States in Hydrogenated a-SiC and a-SiGe Alloys. *Solid State Commun.* **1985**, *54*, 597–601.
- (33) Cody, G. D.; Tiedje, T.; Abeles, B.; Brooks, B.; Goldstein, Y. Disorder and the Optical-Absorption Edge of Hydrogenated Amorphous Silicon. *Phys. Rev. Lett.* **1981**, *47*, 1480–1483.
- (34) Asil, D.; Walker, B. J.; Ehrler, B.; Vaynzof, Y.; Sepe, A.; Bayliss, S.; Sadhanala, A.; Chow, P. C. Y.; Hopkinson, P. E.; Steiner, U.; et al. Role of PbSe Structural Stabilization in Photovoltaic Cells. *Adv. Funct. Mater.* **2015**, *25*, 928–935.
- (35) Guyot-Sionnest, P.; Lhuillier, E.; Liu, H. A Mirage Study of CdSe Colloidal Quantum Dot Films, Urbach Tail, and Surface States. *J. Chem. Phys.* **2012**, *137*, 154704.
- (36) Erslev, P. T.; Chen, H.-Y.; Gao, J.; Beard, M. C.; Frank, A. J.; van de Lagemaat, J.; Johnson, J. C.; Luther, J. M. Sharp Exponential Band Tails in Highly Disordered Lead Sulfide Quantum Dot Arrays. *Phys. Rev. B: Condens. Matter Mater. Phys.* **2012**, *86*, 155313.
- (37) Foos, E. E. The Complex Interaction of Spectroscopic Shifts and Electronic Properties in Semiconductor Nanocrystal Films. *J. Phys. Chem. Lett.* **2013**, *4*, 625–632.
- (38) Luther, J. M.; Law, M.; Song, Q.; Perkins, C. L.; Beard, M. C.; Nozik, A. J. Structural, Optical, and Electrical Properties of Self-Assembled Films of PbSe Nanocrystals Treated with 1,2-Ethanedithiol. *ACS Nano* **2008**, *2*, 271–280.
- (39) Wolcott, A.; Doyeux, V.; Nelson, C. A.; Gearba, R.; Lei, K. W.; Yager, K. G.; Dolocan, A. D.; Williams, K.; Nguyen, D.; Zhu, X.-Y. Anomalous Large Polarization Effect Responsible for Excitonic Red Shifts in PbSe Quantum Dot Solids. *J. Phys. Chem. Lett.* **2011**, *2*, 795–800.
- (40) Tang, J.; Brzozowski, L.; Barkhouse, D. A. R.; Wang, X.; Debnath, R.; Wolowiec, R.; Palmiano, E.; Levina, L.; Pattantyus-

Abraham, A. G.; Jamakosmanovic, D.; et al. Quantum Dot Photo-voltaics in the Extreme Quantum Confinement Regime: The Surface-Chemical Origins of Exceptional Air- and Light-Stability. *ACS Nano* **2010**, *4*, 869–878.

(41) Döllefeld, H.; Weller, H.; Eychmüller, A. Particle-Particle Interactions in Semiconductor Nanocrystal Assemblies. *Nano Lett.* **2001**, *1*, 267–269.

(42) Scheele, M.; Brütting, W.; Schreiber, F. Coupled Organic-Inorganic Nanostructures. *Phys. Chem. Chem. Phys.* **2015**, *17*, 97–111.

(43) Zarghami, M. H.; Liu, Y.; Gibbs, M.; Gebremichael, E.; Webster, C.; Law, M. p-Type PbSe and PbS Quantum Dot Solids Prepared with Short-Chain Acids and Diacids. *ACS Nano* **2010**, *4*, 2475–2485.

(44) Oh, S. J.; Berry, N. E.; Choi, J.-H.; Gaulding, E. A.; Lin, H.; Paik, T.; Diroll, B. T.; Muramoto, S.; Murray, C. B.; Kagan, C. R. Designing High-Performance PbS and PbSe Nanocrystal Electronic Devices through Stepwise, Post-Synthesis, Colloidal Atomic Layer Deposition. *Nano Lett.* **2014**, *14*, 1559–1566.

(45) Zhang, J.; Tolentino, J.; Smith, E. R.; Zhang, J.; Beard, M. C.; Nozik, A. J.; Law, M.; Johnson, J. C. Carrier Transport in PbS and PbSe QD Films Measured by Photoluminescence Quenching. *J. Phys. Chem. C* **2014**, *118*, 16228–16235.

(46) Semonin, O. E.; Johnson, J. C.; Luther, J. M.; Midgett, A. G.; Nozik, A. J.; Beard, M. C. Absolute Photoluminescence Quantum Yields of IR-26 Dye, PbS, and PbSe Quantum Dots. *J. Phys. Chem. Lett.* **2010**, *1*, 2445–2450.

(47) Liu, Y.; Gibbs, M.; Puthussery, J.; Gaik, S.; Ihly, R.; Hillhouse, H. W.; Law, M. Dependence of Carrier Mobility on Nanocrystal Size and Ligand Length in PbSe Nanocrystal Solids. *Nano Lett.* **2010**, *10*, 1960–1969.

(48) Scheele, M.; Engel, J. H.; Ferry, V. E.; Hanifi, D.; Liu, Y.; Alivisatos, A. P. Nonmonotonic Size Dependence in the Hole Mobility of Methoxide-Stabilized PbSe Quantum Dot Solids. *ACS Nano* **2013**, *7*, 6774–6781.

(49) Yazdani, N.; Bozyigit, D.; Yarema, O.; Yarema, M.; Wood, V. Hole Mobility in Nanocrystal Solids as a Function of Constituent Nanocrystal Size. *J. Phys. Chem. Lett.* **2014**, *5*, 3522–3527.

(50) Wehrenberg, B. L.; Yu, D.; Ma, J.; Guyot-Sionnest, P. Conduction in Charged PbSe Nanocrystal Films. *J. Phys. Chem. B* **2005**, *109*, 20192–20199.

(51) Evers, W. H.; Schins, J. M.; Aerts, M.; Kulkarni, A.; Capiod, P.; Berthe, M.; Grandidier, B.; Delerue, C.; van der Zant, H. S. J.; van Overbeek, C.; et al. High Charge Mobility in Two-dimensional Percolative Networks of PbSe Quantum Dots Connected by Atomic Bonds. *Nat. Commun.* **2015**, *6*, 8195.

(52) Murphy, J. E.; Beard, M. C.; Nozik, A. J. Time-Resolved Photoconductivity of PbSe Nanocrystal Arrays. *J. Phys. Chem. B* **2006**, *110*, 25455–25461.

(53) Talgorn, E.; Gao, Y.; Aerts, M.; Kunneman, L. T.; Schins, J. M.; Savenije, T. J.; van Huis, M. A.; van der Zant, H. S. J.; Houtepen, A. J.; Siebbeles, L. D. A. Unity Quantum Yield of Photogenerated Charges and Band-like Transport in Quantum-dot Solids. *Nat. Nanotechnol.* **2011**, *6*, 733–739.

(54) Osedach, T. P.; Zhao, N.; Andrew, T. L.; Brown, P. R.; Wanger, D. D.; Strasfeld, D. B.; Chang, L.-Y.; Bawendi, M. G.; Bulović, V. Bias-Stress Effect in 1,2-Ethanedithiol-Treated PbS Quantum Dot Field-Effect Transistors. *ACS Nano* **2012**, *6*, 3121–3127.

(55) Narayan, T. C.; Miyakai, T.; Seki, S.; Dincă, M. High Charge Mobility in a Tetrathiafulvalene-Based Microporous Metal-Organic Framework. *J. Am. Chem. Soc.* **2012**, *134*, 12932–12935.

(56) Weidman, M. C.; Beck, M. E.; Hoffman, R. S.; Prins, F.; Tisdale, W. A. Monodisperse, Air-Stable PbS Nanocrystals via Precursor Stoichiometry Control. *ACS Nano* **2014**, *8*, 6363–6371.

(57) Melby, L. R.; Hartzler, H. D.; Sheppard, W. A. Improved Synthesis of Tetrathiafulvalene. *J. Org. Chem.* **1974**, *39*, 2456–2458.